PAPER

Subcellular features revealed on unfixed rat brain sections by phase imaging

H.-Y. Nie,*[ab] A. R. Taylor,[c] W. M. Lau[a] and D. F. MacFabe[c]

For sectioned biologic tissues, atomic force microscopy (AFM) topographic images alone hardly provide adequate information leading to revealing biological structures. We demonstrate that phase imaging in amplitude-modulation AFM is a powerful tool in mapping structures present on the surface of unfixed rat brains sections. The contrast in phase images is originated from the difference in mechanical properties between biological structures. Visualization of the native state of biological structures by way of their mechanical properties provides a complementary technique to more traditional imaging techniques such as optical and electron microscopy.

1. Introduction

Imaging of a sample is all about generation of contrast in detected signals over the scanned area from the interaction between the sample and a beam of light in an optical microscope or electron in an electron microscope. Optical microscopy[1,2] and electron microscopy[3,4] are the two most used conventional techniques for imaging biological tissues usually stained with contrast-making agents.[5] For example, for optical microscopy, biological tissue samples are stained with an appropriate agent that has a functional group anchoring to specific molecules and a functional group that either shows a distinctive color, produces an enzyme linked reaction product or emits fluorescence; thus one can use an optical microscope to map the distribution of the targeted molecules.[1,2] When using an electron microscope, an electron-blocking element, usually a heavy metal such as osmium[3] or lead[4] (in the form of their oxides), is added to the sample so that electron beam would receive more resistance at the sites (molecules) where the metal ions are localized, showing contrast for molecules that are selectively bound to the metal ions.

Atomic force microscopy (AFM)[6] is a mechanical probe technique capable of mapping real-space 3-dimensional surface morphology.[7,8] The interaction between the sample surface and the sharp probe tip ($\sim$10 nm in radius at the tip apex) at the free end of a force-sensing cantilever with an optical beam detection scheme provides a feedback mechanism for probing the morphology of the surface. In the dynamic force AFM mode, the tip–sample interaction is controlled by maintaining a reduced amplitude of a vibrating cantilever driven by a piezo element while the tip scans the sample surface. Under this feedback mechanism, the phase lag between the vibrating cantilever detected by the photodetector and the driver signal, referred to as phase shift, is sensitive to both mechanical and chemical properties of the sample.[9–15] Mapping of the phase shift (simultaneously with the topographic image), known as a phase imaging technique, has found applications in differentiating composites having different mechanical and/or chemical properties. For example, it has been demonstrated that phase imaging is capable of revealing *Salmonella typhimurium* encapsulated in extracellular polymeric substances (EPS) due to the different viscoelastic properties between the covering EPS and the underneath bacterium.[16] The direct source for contrasts in phase images obtained in air is from the energy (from the vibrating probe tip) dissipated in the sample surface, whose mechanical properties contribute to the dissipation energy through elastic and/or inelastic deformation.[14,17]

There is a need to develop novel brain imaging techniques to complement traditional immunohistochemical and biochemical methods (using optical and electron microscopes) to localize multiple lipids and other biomolecules in clinical and basic neuroscience. Further to this, we are exploring the use of AFM coupled with time-of-flight secondary ion mass spectrometry (ToF-SIMS),[18–20] with the above traditional techniques to examine neuro-inflammatory, oxidative stress and altered lipid profiles from tissue samples in a rodent model of autism spectrum disorders,[21–23] where emerging evidence suggests autism as a systemic disorder of lipid metabolism resulting in altered membrane fluidity.[24–27]

We have briefly reported the striking contrast observed in phase images, which reveals subcellular features on unfixed rat brain sections, reflecting totally different mechanical properties between the domains rich in fatty acids and the dried cytoplasm consisting of salts and proteins.[18] Therefore, information

[a]*Surface Science Western, The University of Western Ontario, 999 Collip Circle, London, Ontario, N6G 0J3, Canada. E-mail: hnie@uwo.ca*
[b]*Department of Physics and Astronomy, The University of Western Ontario, London, Ontario, N6A 3K7, Canada*
[c]*The Kilee Patchell-Evans Autism Research Group, Departments of Psychology and Psychiatry, Division of Developmental Disabilities, Shulich School of Medicine and Dentistry, The University of Western Ontario, Room 9244, SSC, London, Ontario, N6A 5C2, Canada*

inaccessible to the two more traditional techniques (optical microscopy and electron microscopy) becomes available *via* phase imaging. In this article, we demonstrate that phase imaging visualizes subcellular features present on unfixed rat brain sections *via* the difference in their mechanical properties. We show that compliant composites have a smaller phase shift than rigid ones.

2. Experimental

Adult male Long-Evans rats were sacrificed by decapitation, with procedures completed in accordance with guidelines of the Canadian Council on Animal Care (CCAC) and approved by the University of Western Ontario Animal Use Committee.[21–23] Unfixed brains were rapidly removed and immediately frozen at −70 °C with OCT-embedding for cryoprotection (OCT stands for optimum cold temperature compound, which is a mixture of poly(vinyl alcohol), poly(ethylene glycol) and other non-reactive ingredients). Coronal sections of dorsal hippocampal formation, adjacent neocortex and external capsule white matter were cut from the OCT-embedded brains in a cryostat operated at −20 °C and were placed on glass slides.[18–23] The thickness of the rat sections was 5 μm. Fig. 1 shows a ToF-SIMS ion image overlaid with CNO$^-$ (a characteristic ion fragment for peptide bonds) and $C_{27}H_{45}O^-$ (deprotonated cholesterol molecular ion fragment) for visualization of the hippocampal formation for the sectioned rat brain. The AFM images presented in this article were collected in areas of (a) *Cornu Ammonis* (CA) for pyramidal neurons, (b) stratum radiatum (indicated by the symbol * in Fig. 1) for a region enriched with Schaffer collaterals, which are axons projecting from CA3 pyramidal neurons and (c) external capsule
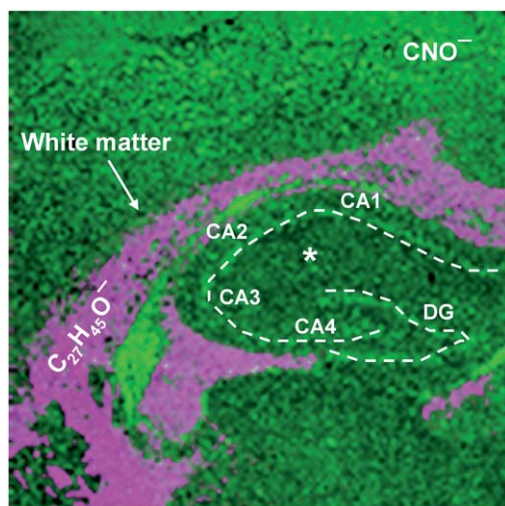

Fig. 1 A ToF-SIMS ion image (scan area: 5 mm × 5 mm) of CNO$^-$ (in green, representing peptide bonds) and $C_{27}H_{45}O^-$ (in pink, deprotonated cholesterol molecular ion) for the sectioned rat brain, showing the hippocampal formation. The external capsule white matter area is represented by the cholesterol molecular ion fragment. The CNO$^-$ ion fragment makes barely visible contrast for pyramidal neurons in the CA1–4 and dentate gyrus (DG) areas, which are guided by inserted dashed lines. Stratum radiatum (str. rad.), a test region for AFM imaging, is marked by the symbol *.

white matter for cholesterol. Details about ToF-SIMS imaging of sectioned rat brains are published elsewhere.[18,20]

The dynamic force mode of a Park Systems XE-100 AFM was used in this study. In this mode, a cantilever with a nominal spring constant of 40 N m^{-1} and a resonant frequency of 300 kHz (NSC15, Mikro Masch) was vibrated and its reduced amplitude A (*e.g.*, 70% of A_0, the amplitude in free space, where there are no tip–sample interactions) was used as the feedback parameter to image the surface morphology. In this amplitude-modulation AFM (AM-AFM or tapping) mode, a phase shift of the cantilever detected by the photodetector is the phase lag relative to that of the piezo driver. The phase shift is a measure of surface properties (*e.g.*, mechanical properties and surface chemistry) that cause different interactions between the AFM tip and the sample surface. In our experiments for imaging, unless stated otherwise, the driving frequency was set slightly below the resonant frequency. We use the as-obtained phase shift when we show a sectional profile from a phase image, which results in an offset but does not alter the contrast. In the case of collecting force–, phase– and amplitude–distance curves, the driving frequency was set at the resonant frequency (so that phase shift should be 90° when the tip was in free space). The AFM experiments were carried out in air at room temperature with a relative humidity of ∼40%.

Cantilever sensitivity was estimated by moving the tip certain distance into a hard surface (*e.g.*, a Si wafer) and monitoring the response of the photodetector. With an estimated cantilever sensitivity of 70 ± 5 V μm^{-1} and the nominal spring constant of the cantilever, the photodetector output data were converted to force (nN). The amplitude of a vibrating cantilever was obtained by pushing it onto a Si wafer surface: the amplitude decreases linearly with decreasing tip–sample distance.[8,28]

3. Results and discussion

We located pyramidal neurons concentrated in the CA1–4 areas, from which we collected a number of AFM images. Shown in Fig. 2 are topographic and phase images obtained on such a pyramidal neuron in the CA1 area in the hippocampal formation on a sectioned rat brain.[18–20] Although the topographic image in Fig. 2a provides information as how the sectioned tissue surface looks like after being dried in air, it hardly reveals biological structures of the rat brain section. A typical profile is shown below the image, which indicates the height (Fig. 2a) or phase shift (Fig. 2b) range of the image.

By contrast, as shown in Fig. 2b, the phase image displays striking contrasts of phase shift over the surface of the sectioned rat brain. Because those phase contrasts resemble some of the subcellular features of neurons, we believe that they are originated from different molecules presented in the observed domains on the sectioned surface. The profile shown below the image indicates that the phase shift varies between −58° and 24°, suggesting that there exist totally different material properties between the subcellular features and the surrounding cytoplasm. The darker (smaller phase shift) domains observed in the phase image are round with sizes ranging from 0.1 to 1 μm. Those sizes are consistent with that of typical subcellular features such as mitochondria, Golgi apparatus, endoplasmic reticulum and nucleus.[3,29] These subcellular domains are indeed rich in
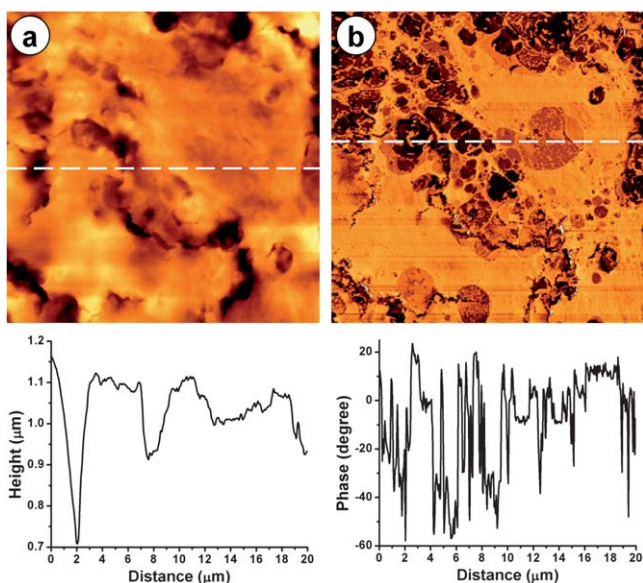
Fig. 2 Topographic (a) and phase (b) images (scan area: 10 μm × 10 μm) for a pyramidal neuron in the CA1 area on a sectioned rat brain. A profile from each image isolated from the dashed line is shown below the image. The height range is 1.2 μm and the phase shift range is 82° (−58° to 24°).

phospholipids.[18] When dried in air, the behavior and properties of lipids should be quite different from those of salts and proteins: lipid molecules would rarely change their mechanical properties because of the lack of water content in them, while salts and proteins would be desiccated.

Shown in Fig. 3 are AFM topographic and phase images obtained in the area of stratum radiatum (as indicated by the
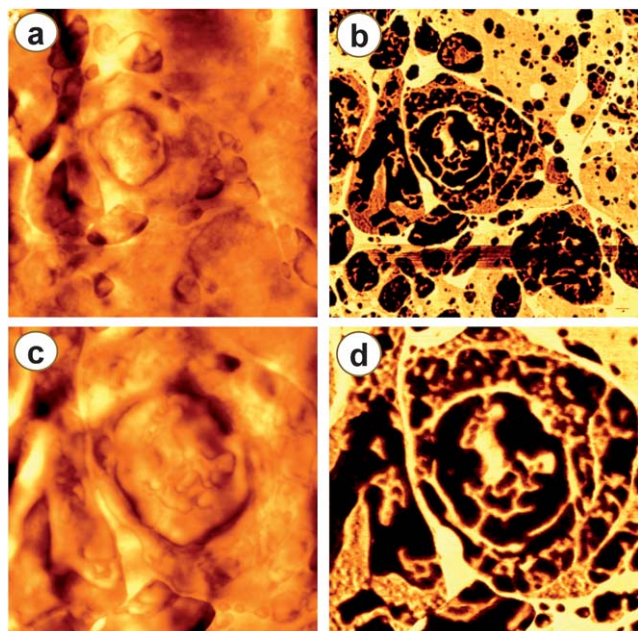
symbol * in Fig. 1). The topographic image shown in Fig. 3a does not provide much information on structures of the sectioned tissue. In Fig. 3b, however, the phase image shows clearly structures on the sectioned stratum radiatum. Although not conclusive, these structures are consistent with cross sections of Schaffer collaterals, which are axons from CA3 pyramidal neurons.[30] Shown in Fig. 3c and 3d are magnifications of Fig. 3a and 3b, respectively, and they provide a close up of the observed structures.

There appear to be four contrasts in the phase image shown in Fig. 3b, which suggests that there should be different composites that give rise to the different compliance as accessed by the phase imaging technique. Phase shift measurements thus serve to reveal biological structures as different structures usually consist of different biomolecular profiles.

Another example is shown in Fig. 4, where the AFM topographic image (Fig. 4a) reveals the crystallization of cholesterol molecules (as verified by ToF-SIMS investigations[18]) and the phase image (Fig. 4b) suggests that the phase shift on the crystallized cholesterol is much higher than that on other part of the sectioned rat brain. This is because the crystallized cholesterol molecules are perhaps among the most rigid lipid structure presented on a sectioned rat brain.[31,32]

The topographic image in Fig. 4a shows that there are crystalline structures covering the white matter area. These features are due to crystallization of cholesterol molecules as they are especially rich in the white matter region. One interesting observation is that cholesterol-rich areas always protrude ∼2 μm as measured with a stylus profiler capable of mapping the entire sectioned rat brain (not shown). We speculate that when the biological tissue is being cut, the surface is flat. However, after the sectioned tissue was desiccated in air, the area with increased water content would contract while the cholesterol-rich area might not be affected by the drying process because of the lack of water content in that area.

We noticed in our experiments that the phase contrast on sectioned rat brains probed using commercial AFM tips (made of single crystalline silicon covered with its native oxide) was reproducible and tip contamination rarely happened. Our experimental results thus clarified that phase imaging is a robust technique for visualization of biological structure with ample spatial resolution (by way of differentiating mechanical properties).
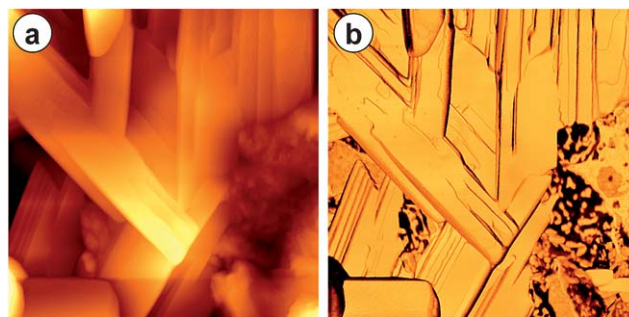

Fig. 3 Topographic (a,c) and phase (b,d) images obtained in the stratum radiatum area of the hippocampal formation on a sectioned rat brain. The scan area for (a) and (b) is 10 μm × 10 μm and for (c) and (d) is 5 μm × 5 μm, respectively. The height range is 300 nm and the phase shift range is 53° (5° to 58°).

Fig. 4 Topographic (a) and phase (b) images (scan area: 5 μm × 5 μm) obtained on the white matter area of a sectioned rat brain. The height range is 540 nm and the phase shift range is 104° (−56° to 48°).

In order to understand the phase shift contrast observed on the sectioned rat brains, we start from the equation of motion for a vibrating cantilever in free space. In this case, the dynamics of the cantilever can be modeled as a point mass attached to a spring, which may be described as follows:

$$m \frac{d^2 z}{dt^2} + c \frac{dz}{dt} + kz = F_0 \cos \omega t \tag{1}$$

where z is the distance the cantilever traverses, t time, m the mass of the cantilever–tip ensemble, c the damping coefficient for the cantilever moving in a medium, k the spring constant of the cantilever, F_0 and ω the amplitude and angular frequency of the vibrating force produced by the piezo driver attached to the fixed end of the cantilever. With the two definitions of $\omega_0^2 = \frac{k}{m}$ and $c = \frac{m\omega_0}{Q}$, where ω_0 is the angular resonant frequency of the cantilever and Q the quality factor, eqn (1) can be written as:

$$\frac{d^2 z}{dt^2} + \frac{\omega_0}{Q} \frac{dz}{dt} + \omega_0^2 z = \frac{F_0}{m} \cos \omega t \tag{2}$$

This second order non-linear differential equation has a steady-state solution of

$$z = A\cos(\omega t + \phi) \tag{3}$$

with A being the amplitude of the oscillation and ϕ its phase shift relative to the driver signal:

$$A = \frac{F_0/m}{[(\omega_0^2 - \omega^2)^2 + (\omega\omega_0/Q)^2]^{1/2}} \tag{4}$$

$$\tan \phi = \frac{\omega\omega_0/Q}{\omega_0^2 - \omega^2} \tag{5}$$

Shown in Fig. 5 are simulations (shown only in the range of 290–310 kHz) for the amplitude (eqn (4)) and phase shift (eqn (5)) as
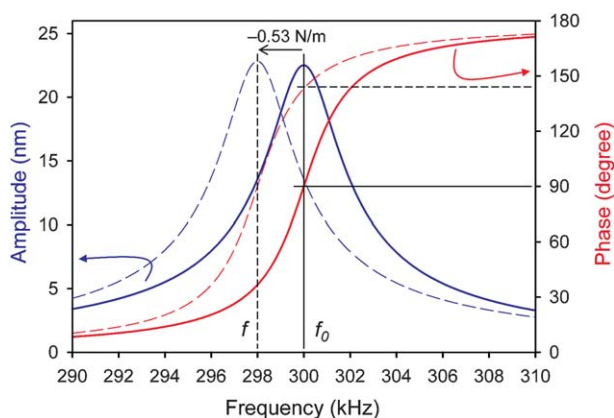

Fig. 5 Simulations of the amplitude and phase shift (solid lines) of a cantilever (resonant frequency $f_0 = 300$ kHz) in free space (solid lines) and with an attractive force having a gradient of -0.53 N m^{-1} exerted on the tip (dashed lines) as a function of the vibrating frequency. The attractive force shifts the resonant frequency to $f = 298$ kHz. When the vibrating frequency is fixed at f_0, the attractive force will change the phase shift from its free-space value of 90° (indicated by the solid horizontal line) to 143° (indicated by the dashed horizontal line).

a function of the vibrating frequency for a cantilever having a spring constant of $k = 40$ N m^{-1} and a resonant frequency of $f_0 = \frac{\omega_0}{2\pi} = 300$ kHz (assuming a quality factor of $Q = 100$ and a driving force of $F_0 = 0.36$ mN). The amplitude changes with the vibrating frequency as a Lorentz oscillator with a peak at the resonant frequency f_0; away from f_0, the amplitude approaches zero. It is also shown in Fig. 5 that the phase shift is 90° at the resonant frequency f_0 and approaches 0° and 180° towards zero and infinity frequency, respectively.

In order to see how the phase shift changes when there are forces exerted on the tip, we need to understand how resonant frequency changes with forces exerted on the tip–cantilever ensemble. The resonant frequency of a cantilever in free space is $f_0 = \sqrt{\frac{k}{m}}$. When there is a force F exerted on the tip, as in the AM-AFM operation, the effective spring constant of the cantilever k' deviates from its spring constant k in free space:

$$k' = k + \frac{dF}{dz} \tag{6}$$

This results in a new resonant frequency f:

$$f = \sqrt{\frac{k + \frac{dF}{dz}}{m}} \tag{7}$$

The force gradient $\frac{dF}{dz}$ is negative in the attractive force region and positive in the repulsive force region, respectively. Hence, there is a decrease (increase) in resonant frequency when the tip encounters attractive (repulsive) forces. It follows that, with a cantilever being vibrated at a fixed frequency, attractive (repulsive) forces result in an increase (decrease) in phase shift, because the new resonant frequency f is now smaller (larger) than the original resonant frequency. Such a situation is shown in the amplitude peak and phase curve depicted with the dashed lines in Fig. 5, where an attractive force with a gradient of -0.53 N m^{-1} results in a new resonant frequency about 2 kHz lower than that in free space.

The above discussion associated with the simulation shown in Fig. 5 may be used to qualitatively describe the trend as how the phase shift changes with forces exerted on a vibrating cantilever. In practical AM-AFM operations with a vibrating amplitude at the order of 60 nm, the situation might be different from the simple simulation shown here.[8,28] In fact, any forces exerted on the tip reduce the vibrating amplitude of the cantilever.[17] As we will see from the results to follow, however, the phase shift measured on the sectioned rat brains appears to support the trend described in Fig. 5.

In AM-AFM mode, the vibrating cantilever is in certain interaction with the sample surface, generating certain amount of phase shift, determined by mechanical properties of the sample, among other properties that result in energy dissipation in the tip–sample interaction.[14,17] On the surface of sectioned rat brains, we have observed that compliant domains always have a smaller phase shift than rigid areas. In order to develop phase imaging as a technique for visualization of biological structures by way of their mechanical properties, we need to clarify why the phase shift is smaller on compliant domains than on more rigid areas.

Since the phase shift in a phase image is only measured at one setpoint, in order to investigate the mechanism for the observed contrast in our phase images, we conducted experiments by moving the tip towards the sample surface to see how the phase shift changes as a function of the tip–sample distance. In order to do this, we first imaged an area on a neuropil in the stratum radiatum area (with a setpoint of $A/A_0 = 75\%$) so that we were able to locate areas of interests, as shown in Fig. 6. The three areas marked as 1, 2 and 3 in Fig. 6b show distinct phase shifts (in order of decreasing phase shift). On each of those specified areas, we collected data at 5 spots and verified the reproducibility of the amplitude–, force– and phase–distance curves. Typical curves obtained on those areas are shown in Fig. 7.

From the amplitude–distance curves in Fig. 7a, one can see that the amplitude decreases linearly with decreasing tip–sample distance on area 1, which is typically observed on a relatively rigid surface.[8,13,28] The distance range where the amplitude decreases with decreasing tip–sample distance is the working distance for the AM-AFM operation. On area 2, the amplitude is only slightly distorted in comparison with that on area 1. It is clear that on area 3, however, the amplitude is distorted from linearity. These amplitude behaviors as a function of the tip–sample distance, as shown in Fig. 7a, indicate that area 3 is the softest one among the three. This is readily confirmed by the force–distance curves in Fig. 7b, from which one sees that the materials located in the three specified areas have different mechanical properties, with area 3 being more compliant than areas 1 and 2. Even though the force was measured with a vibrating cantilever, the portion after the tip mechanically touches the sample surface still reflects the mechanical properties of the sample (because the cantilever ceases vibrating).
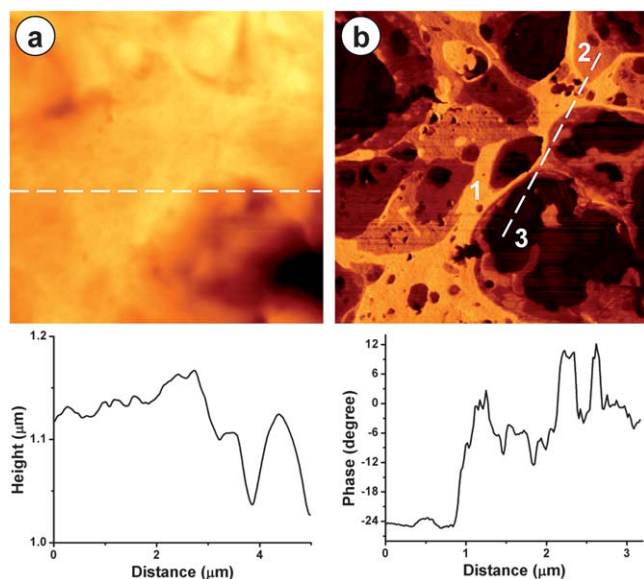

Fig. 6 Topographic (a) and phase (b) images (scan area: 5 μm × 5 μm) obtained in the stratum radiatum area of the hippocampal formation on a sectioned rat brain. The dashed lines in the images indicate the profiles shown below. The three representative areas showing distinct phase contrast are marked 1, 2 and 3, from which variations of the amplitude, phase shift and force against the tip–sample distance were measured and are shown in Fig. 7. The height range is 2.0 μm and the phase range is 40° (−28° to 12°).
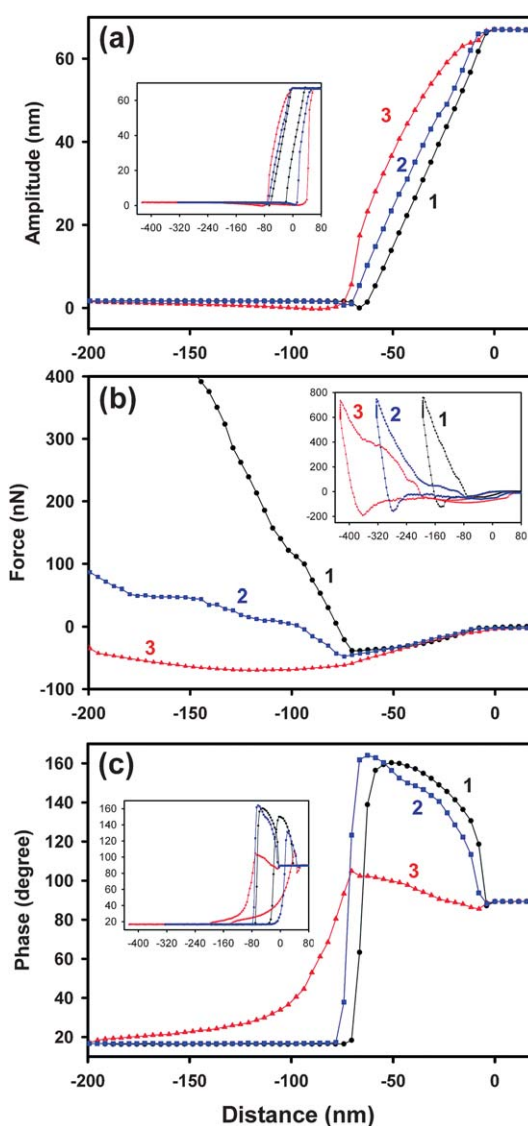

Fig. 7 Curves of the amplitude (a), force (b) and phase (c) vs. the tip–sample distance on the three distinct areas specified in Fig. 6b. The spring constant and resonant frequency of the cantilever used were 40 N m⁻¹ and 310 kHz, respectively. The cantilever was vibrated at its resonant frequency and its quality factor was 600. The speed of the probe tip approaching and retracting from the sample surface was 300 nm s⁻¹. The inserts in (a)–(c) show the amplitude–, force– and phase–distance curves in the full approach and retraction cycle. The phase data in (b) are offset so that they become 90° in free space (the measured value was approximately −20°).

On area 1, it takes the least indentation for the AFM probe to reach a specified force (e.g., ∼750 nN as shown in the inset in Fig. 7b). This shows that the surface is relatively rigid because the repulsive force is established immediately when the tip mechanically touches the surface. Area 2 is more compliant than area 1 since the slope of the force–distance curve obtained on area 2 after the mechanical contact is much smaller than that seen on area 1. Kinks seen in the force–distance curve for area 2 suggest changes in mechanical properties of the material as the AFM tip pushes into the sample. For area 3, one sees that the establishment of repulsive forces needs the tip to further move in for more

than ~150 nm, indicating that the material of area 3 is extremely compliant. A lipid rich material would behave like this: it will yield to the approaching AFM tip. As shown in the inset in Fig. 7b, eventually the AFM tip exerts repulsive forces to area 3, perhaps due to a rigid composite underneath the lipid rich subcellular features.

Shown in Fig. 7c are the phase–distance curves obtained over the three specified areas 1–3 in Fig. 6b. The phase shift is (set to) 90° when the tip is in free space (with tip–sample distance ≧0 nm) because the cantilever is vibrated at its resonant frequency. When the tip approaches the sample surface (with tip–sample distance <0 nm), over the majority of the working distance, the phase shift is larger than 90°, which may be explained by that there are attractive forces exerted on the AFM tip as described in Fig. 5. With decreasing tip–sample distance, repulsive forces eventually become to dominate the tip–sample interaction, making the phase shift smaller than 90°. This situation is well demonstrated on rather rigid surfaces such as a Si wafer.[8,13]

On area 1, the phase shift increases with decreasing tip–sample distance, up to ~160°, before the tip mechanically touches the sample, where it falls towards a fixed value (~20°, which was perhaps due to the AFM system we used, not necessarily physically meaningful). The phase shift variation against the tip–sample distance observed on area 2 resembles that on area 1, except for that it has a slightly smaller value in most of the working distance.

By contrast, the phase shift measured on area 3 is much smaller than those on the other two areas. The phase shift is not that far from 90° in the working distance, suggesting that the resonant frequency is not changed too much from that in free space. This implies that the attractive force gradient on area 3 is much smaller than those on the more rigid areas 1 and 2. Another significant difference observed on area 3 is that the phase shift does not reach the fixed value (~20°) even when the tip pushes to the surface for more than 100 nm in comparison with those observed on areas 1 and 2 (Fig. 7c), which is a clear indication that area 3 is a highly compliant material. On the basis of the results shown in Fig. 7b and 7c, it is verified that a brighter (larger phase shift) area in a phase image corresponds to a stiffer material and a darker (smaller phase shift) area represents a more compliant material.

Fig. 8 can be used to explain the contrasts observed in the phase images presented in this article. In AM-AFM mode, a reduced amplitude is kept constant during scanning; the horizontal line in Fig. 8a depicts a setpoint of $A/A_0 = 75\%$ for the images shown in Fig. 6. This horizontal line intersects each of the three amplitude–distance curves. The three vertical lines from the three intersections at the amplitude–distance curves in Fig. 8a point to the three phase–distance curves in Fig. 8b, determining the phase shift measured in the specified areas 1–3 in Fig. 6b. With the phase shift in free space being set to 90°, comparison between the phase shift values indicated by the dashed lines in Fig. 8b and those measured in areas 1–3 in Fig. 6b leads to the estimation of an offset of ~120° for our AFM system.

In the particular case shown Fig. 8, although the phase shift varies to certain level when we change the setpoint, the contrast for areas 1 and 2 in phase imaging will not reverse as long as the setpoint A/A_0 is more than 30%. This is estimated by finding the reduced amplitude for area 2 (in Fig. 8a) corresponding to the
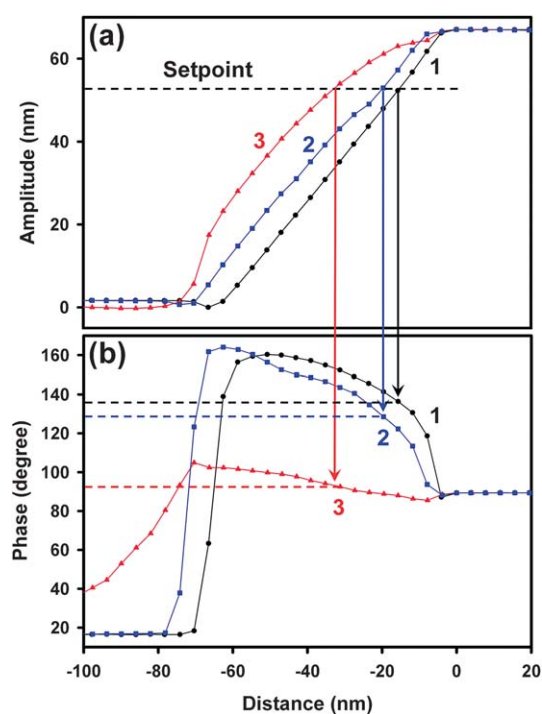

Fig. 8 Amplitude–distance (a) and phase–distance (b) curves used for illustrating the setpoint ($A/A_0 = 75\%$) represented by the dashed line in (a) and the corresponding phase shift in areas 1–3 indicated by the three vertical arrow lines and the three dashed lines in (b).

cross point between the two phase–distance lines (in Fig. 8b, at round −55 nm in distance). When the setpoint becomes less than this value, which is impractical in AM-AFM, according to Fig. 8, the phase shift in area 2 is supposed to become larger than that in area 1. However, the phase shift for area 3 remains to be the smallest. Therefore, for practical AM-AFM operation conditions, where the setpoint A/A_0 is most likely in the proximity of 70% and rarely out of the range of 80–40%, the contrast in phase images will not reverse. This is important in ensuring the reproducibility of identification of biological structures by way of their mechanical properties.

4. Conclusions

We demonstrated that the phase shift of a vibrating cantilever in amplitude-modulation atomic force microscopy is sensitive to subcellular features presented on unfixed rat brain sections. The striking contrast observed between subcellular features and, for example, surrounding cytoplasm is due to their different mechanical properties, which is a reflection of their molecular constituents. With analyses of amplitude–, force– and phase–distance curves, we clarified that phase imaging is a robust contrast-making technique for biological tissues: the phase shift of compliant domains is always smaller than that of more rigid areas. Therefore, phase imaging technique provides a new imaging mechanism for subcellular features which is complementary to more conventional optical and electron microscopy. It is especially advantageous that phase imaging probes biological structures with a spatial resolution that is mainly limited by the probe size (which is <10 nm in radius). Under way are

applications of the phase imaging technique in examination of sectioned rat brains for potential membrane alterations in animal models of autism and related neurological disorders.

Acknowledgements

Reference

1 B. P. Lane and D. L. Europa, *J. Histochem. Cytochem.*, 1965, **13**, 579–582.
2 M. C. Brundrett, D. E. Enstone and C. A. Peterson, *Protoplasma*, 1988, **146**, 133–142.
3 M. L. Watson, *J. Biophysic. Biochem. Cytol.*, 1958, **4**, 475–478.
4 E. S. Reynolds, *J. Cell Biol.*, 1963, **17**, 208–212.
5 S. M. Hsu, L. Raine and H. Fanger, *J. Histochem. Cytochem.*, 1981, **29**, 577–580.
6 G. Binnig, C. F. Quate and C. Gerber, *Phys. Rev. Lett.*, 1986, **56**, 930–933.
7 S. N. Magonov, V. Elings and M.-H. Whangbo, *Surf. Sci.*, 1997, **375**, L385–L391.
8 R. García and R. Pérez, *Surf. Sci. Rep.*, 2002, **47**, 197–301.
9 J. P. Cleveland, B. Anczykowski, A. E. Schmid and V. B. Elings, *Appl. Phys. Lett.*, 1998, **72**, 2613–2615.
10 J. Tamayo and R. García, *Appl. Phys. Lett.*, 1998, **73**, 2926–2928.
11 T. R. Rodriguez and R. García, *Appl. Phys. Lett.*, 2004, **84**, 449–451.
12 M. Kober, E. Sahagun, M. Fuss, F. Briones, M. Luna and J. J. Saenz, *Phys. Status Solidi RRL*, 2008, **2**, 138–140.
13 J. Tamayo and R. García, *Langmuir*, 1996, **12**, 4430–4435.
14 N. F. Martínez and R. García, *Nanotechnology*, 2006, **17**, S167–S172.
15 Y. F. Dufrêne, *Analyst*, 2008, **133**, 297–301.
16 Z. Y. Suo, X. H. Yang, R. Avci, L. Kellerman, D. W. Pascual, M. Fries and A. Steele, *Langmuir*, 2007, **23**, 1365–1374.
17 R. García, R. Magerle and R. Perez, *Nat. Mater.*, 2007, **6**, 405–411.
18 H.-Y. Nie, J. T. Francis, A. R. Taylor, M. J. Walzak, W. H. Chang, D. F. MacFabe and W. M. Lau, *Appl. Surf. Sci.*, 2008, **255**, 1079–1083.
19 J. T. Francis, H.-Y. Nie, A. R. Taylor, M. J. Walzak, W. H. Chang, D. F. MacFabe and W. M. Lau, *Appl. Surf. Sci.*, 2008, **255**, 1126–1130.
20 H.-Y. Nie, A. R. Taylor, J. T. Francis, M. J. Walzak, W. M. Lau and D. F. MacFabe, *Surf. Interface Anal.*, 2011, **43**, 358–362.
21 D. F. MacFabe, D. P. Cain, K. Rodriguez-Capote, A. E. Franklin, J. E. Hoffman, F. Boon, A. R. Taylor, M. Kavaliers and K.-P. Ossenkopp, *Behav. Brain Res.*, 2007, **176**, 149–169.
22 D. F. MacFabe, K. Rodríguez-Capote, J. E. Hoffman, A. E. Franklin, Y. Mohammad-Asef, A. R. Taylor, F. Boon, D. P. Cain, M. Kavaliers, F. Possmayer and K.-P. Ossenkopp, *Am. J. Biochem. Biotechnol.*, 2008, **4**, 146–166.
23 D. F. MacFabe, N. E. Cain, F. Boon, K.-P. Ossenkopp and D. P. Cain, *Behav. Brain Res.*, 2010, **217**, 47–54.
24 A. Chauhan and V. Chauhan, *Pathophysiology*, 2006, **13**, 171–181.
25 M. R. Herbert, *Curr. Opin. Neurol.*, 2010, **23**, 103–110.
26 A. Aneja and E. Tierney, *Int. Rev. Psychiatry*, 2008, **20**, 165–170.
27 R. H. Thomas, K. A. Foley, J. R. Mepham, L. J. Tichenoff, F. Possmayer and D. F. MacFabe, *J. Neurochem.*, 2010, **113**, 515–529.
28 A. Kühle, A. H. Sørensen and J. Bohr, *J. Appl. Phys.*, 1997, **81**, 6562–6569.
29 K. H. Pfenninger, L. Ellis, M. P. Johnson, L. B. Friedman and S. Somlo, *Cell*, 1983, **35**, 573–584.
30 Y. Nakamura, H. Tamura, K. Horinouchi and S. Shiosaka, *J. Cell Sci.*, 2006, **119**, 1341–1349.
31 D. Weihs, J. Schmidt, I. Goldiner, D. Danino, M. Rubin, Y. Talmon and F. M. Konikoff, *J. Lipid Res.*, 2005, **46**, 942–948.
32 C. Krafft, S. B. Sobottka, G. Schackert and R. Salzer, *Analyst*, 2005, **130**, 1070–1077.